Development and Operation Control of a Switched-Reluctance Motor Driven Flywheel

Chi-Yuan Ho, Jung-Chi Wang, Kai-Wei Hu, *Member, IEEE*, and Chang-Ming Liaw, *Member, IEEE*

***Abstract*—This paper presents the development of a switched-reluctance machine (SRM) driven flywheel system, its charging/discharging controls, and performance evaluations. By properly setting and tuning the winding commutation instant, the same SRM can be operated as a motor and a generator in the SRM-driven flywheel system with satisfactory performances. Moreover, the hysteresis current controlled pulsewidth modulation scheme with hard freewheeling and the commutation angle dynamic shift controller are proposed to enhance the flywheel discharging generating performance. For interfacing the flywheel system to the dc microgrid, a half-bridge bidirectional dc–dc interface converter is developed. It is operated in a buck mode under flywheel charging and in a boost mode under flywheel discharging. The dynamic modeling and controller design are conducted to yield well-regulated dc output voltage under varying flywheel-driven switched-reluctance generator (SRG) speed. Finally, the measured results are given to verify the performances of the established flywheel and its interconnected operation to a wind SRG-based dc microgrid.**

***Index Terms*—Commutation tuning, energy storage system, flywheel, interface converter, microgrid, switched-reluctance machine (SRM).**

NOMENCLATURE

$G_{cc}(s)$	Voltage tracking error controller.
$G_{cs}(s)$	Dynamic shift controller.
$G_{cv}(s)$	Voltage feedback controller.
$G_{c\omega}(s)$	Flywheel speed feedback controller.
$H_{\mathrm{LP}}(s)$	Low-pass filter.
P_d	Interface converter output power.
P_{df}	Flywheel charging/discharging power.
P_g	SRM air-gap power.
v_b	Battery bank voltage.
v_d	Interface converter output voltage.
v_{dc}	Microgrid dc-link voltage.
v_{df}	Flywheel dc-link voltage.
β	Commutation shift angle.
β_m	Flywheel motor mode commutation angle.
β_g	Flywheel generator mode commutation angle.

Manuscript received June 30, 2017; revised September 15, 2017 and January 13, 2018; accepted February 22, 2018. Date of publication March 9, 2018; date of current version November 19, 2018. Recommended for publication by Associate Editor F.-J. Lin. *(Corresponding author: Chang-Ming Liaw.)*

C.-Y. Ho, K.-W. Hu, and C.-M. Liaw are with the Department of Electrical Engineering, National Tsing Hua University, Hsinchu 300, Taiwan (e-mail:

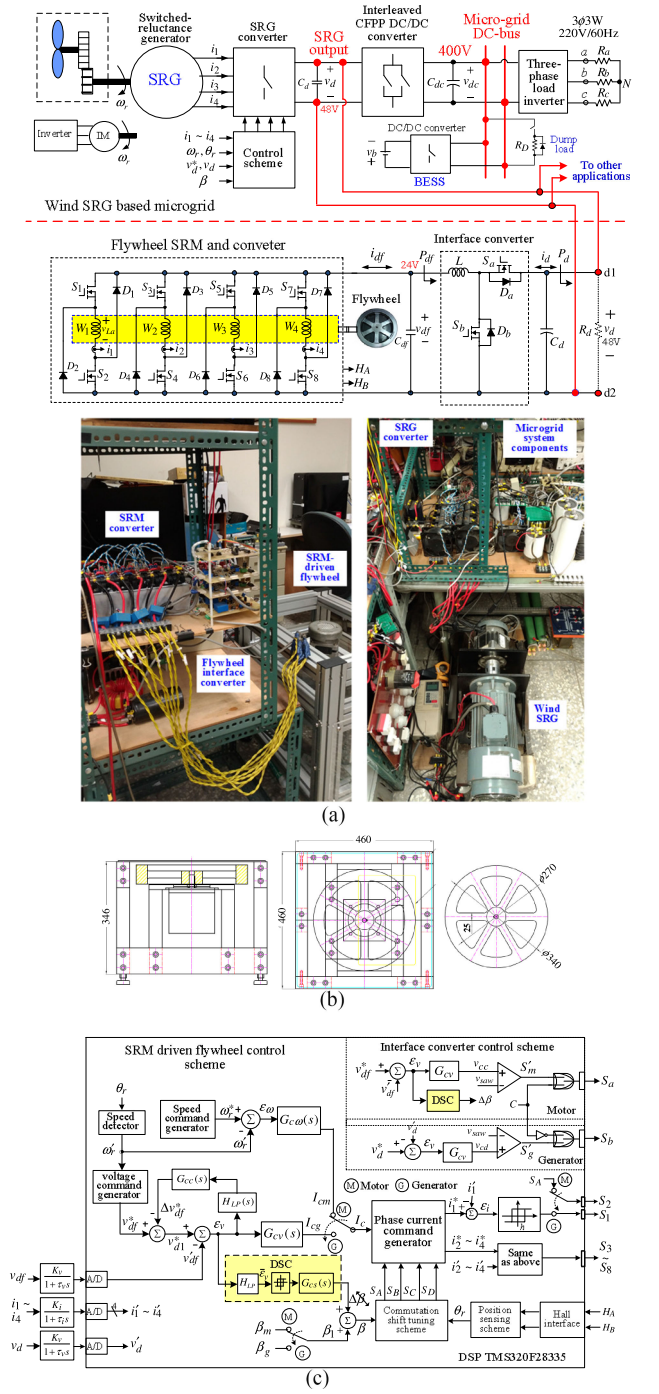

Fig. 1. Configuration and control schemes of the developed SRM-driven flywheel system. (a) Schematic and photos. (b) Dimensions of the constructed flywheel. (c) Control scheme.

current waveform. The typical improvement studies for improving its driving performance include: 1) motor design [20], [21]; 2) current control [22]; 3) speed control [23]; 4) commutation shift control [24]–[26]; and 5) voltage boosting [27], [28]. The commutation shift and voltage boosting are the two effective approaches to enhance the SRM drive operating characteristics in high speeds.

The SRM can also be operated as a generator by properly setting its winding current commutation instant at the negative winding inductance slope region. Owing to the merits of cogging ripple free feature and good power generating capability, the SRM is suited to be operated as a generator. The typical example applications include variable speed wind generators [29], [30] and integrated starter/generator [31] in electric vehicles. However, switched-reluctance generator (SRG) generation performance is also highly affected by many factors. The detailed analyses can be found in [32]–[34]. Among these, the proper commutation setting is the most important one affecting the winding current waveforms and the developed power of an SRG. Not surprisingly, the winding currents pulsewidth modulation (PWM) switching control is easy to fail and enter a single-pulse mode under higher speed and/or heavier load. The generating control variables will be dominated by commutation instants. As the other commonly employed motors, by properly setting the winding commutation instant for an SRM, it can be operated as a motor and a generator for being the actuator of the flywheel. In this paper, some key technologies are developed for improving the SRM-driven flywheel charging/discharging performances.

For an energy storage device, the bidirectional interface converter is needed for conducting the discharging and charging operations. Till now, there already are several bidirectional dc–dc converters [35]–[39] being applied to electrical vehicles and renewable power systems. In the developed SRM-driven flywheel, a one-leg bidirectional dc–dc converter is designed and used as its interface to the system common dc bus.

This paper presents the development of an experimental SRM-driven flywheel system and performs its charging and discharging operation controls. For interfacing the flywheel system to the wind SRG output, a half-bridge bidirectional dc–dc interface converter is developed. It is operated in a buck mode under a flywheel charging mode and in a boost mode under a flywheel discharging mode. In addition to the charging operation mode, the flywheel discharging performances are enhanced via the proposed hysteresis current controlled PWM (HCCPWM) scheme, dynamic commutation shift approach, proper voltage command setting, etc. Some measured results are given to verify the operation characteristics of the established SRM-driven flywheel. The established flywheel followed by an interfaced converter is first verified experimentally by its charging and discharging operation characteristics. Then, the SRM-driven flywheel system is connected to a wind SRG-based dc microgrid to express the energy support application potential by some measured results. The flywheel can be charged from the microgrid dc bus to establish its running speed. Conversely, the flywheel can discharge the stored energy to power the microgrid. Specifically speaking, the performance enhancement approaches presented in this paper for an SRM-driven flywheel include

1) SRM/SRG key issues explorations in Section II-B;
2) Commutation shifting under SRM driving operation in Sections III-C and V-A;
3) Commutation shifting under SRG discharging operation in Sections III-C and V-B;
4) Flywheel bidirectional interface converter establishment and control in Section IV; and

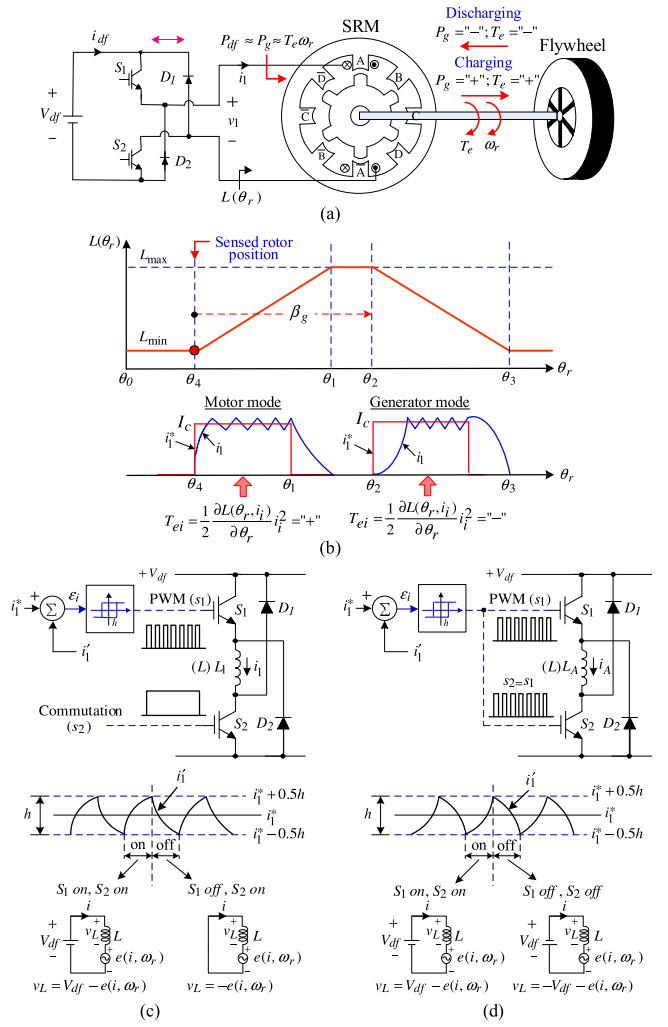

Fig. 2. Configuration and operation controls for the SRM-driven flywheel. (a) System configuration. (b) Winding inductance profile and operation modes. (c) Current control PWM scheme and equivalent circuits in the motor mode. (d) Current control PWM scheme and equivalent circuits in the generator mode.

5) The interconnection operation control of the developed SRM-driven flywheel to a wind SRG-based microgrid in Section VI.

The presented approaches are helpful for establishing a high-performance SRM-driven flywheel and achieving its successful applications.

II. System Configuration and Switched-Reluctance Machine

A. System Configuration

1) SRM-Driven Flywheel: Fig. 1(a) shows the configuration and photos of the established SRM-driven flywheel system. The flywheel output v_{df} (24 V) is processed through a one-leg bilateral dc–dc interface converter (L, S_a, D_a, S_b, D_b) to establish the boosted dc-link voltage of v_d (48 V). It can be used to provide energy buffer for the dc microgrid as shown or for other systems, such as elevator, uninterruptable power supply, etc. The dimensions of the constructed SRM flywheel are shown in Fig. 1(b). Although it lacks practicality without sealed in vacuum environment and levitated bearing, it can be applied to conduct the SRM-driven flywheel operation study. The developed technologies are unified and can be directly applied to a practical flywheel.

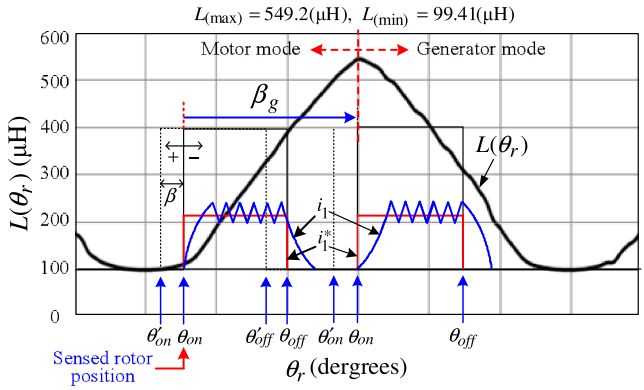

Fig. 3. Measured winding inductance profile and the defined key variables related to the commutation processes of SRM and SRG.

Since the SRM cannot be popularly purchased like other commercialized three-phase motors, an available one with ratings of 24 V/490 W/6000 r/min is employed to be the flywheel actuator. The designs of the SRM converter and the followed interface converter are easy to update according to the specified rated voltages. The proposed flywheel control scheme is depicted in Fig. 1(c). The designs of its constituted controllers are presented in Sections III and IV.

2) Microgrid: An available dc microgrid shown in the upper part of Fig. 1(a) consists of a wind SRG ($v_d = 48$ V), a followed interleaved current-fed push–pull (CFPP) isolated boost converter (400 V), and a three-phase load inverter. To preserve the energy supplying quality, a battery energy storage system is connected to the microgrid common dc-bus ($v_{\rm dc} = 400$ V) via a bidirectional dc–dc converter. As shown in Fig. 1(a), by interconnecting the developed SRM flywheel with the microgrid, the charging from the microgrid to accelerate the flywheel, and conversely, the discharging of flywheel stored energy to support the microgrid can all be successfully performed.

B. Switched-Reluctance Machine and Its Motoring/Generating Operations

1) SRM Governing Equations: By neglecting the coupling effect between phases and assuming a linear magnetic circuit, the phase winding voltage equation of an SRM can be expressed as

$$v = R_s i + \frac{d\lambda(\theta_r, i)}{dt} \triangleq R_s i + L(\theta_r, i)\frac{di}{dt} + \frac{\partial L(\theta_r, i)}{\partial \theta_r} i\,\omega_r$$
$$\triangleq R_s i + L(\theta_r, i)\frac{di}{dt} + e(\theta_r, i, \omega_r) \quad (1)$$

where v = winding terminal voltage, R_s = winding resistance, i = winding current, $\lambda(\theta_r, i)$ = winding flux linkage, θ_r = rotor position, $L(\theta_r, i)$ = winding inductance, ω_r = rotor speed, and $e(\theta_r, i, \omega_r)$ = back electromagnetic force (EMF).

The per-phase developed torque can be derived from the field energy or co-energy; hence, the composite torque and mechanical equation of an SRM drive can be written as

$$T_e = \sum_{i=1}^{N} T_{ei} = \frac{1}{2}\sum_{i=1}^{N} \frac{\partial L_i(\theta_r, i_i)}{\partial \theta_r} i_i^2 = T_L + B\omega_r + J\frac{d\omega_r}{dt} \tag{2}$$

where T_L = load torque, B = total coefficient of friction, J = total moment of inertia, and N = phase number.

2) Key Issues of SRM and SRG: Some observations can be made from (1) and (2):

1) The back EMF of an SRM is dependent on $\partial L(\theta_r, i)/\partial\theta_r$, i, and ω_r. Hence, different to other motors, it is zero as $i = 0$. The back EMF is increased with i and ω_r to limit the winding current control performance under high speeds. Commutation shift and voltage boosting are the effective approaches to improve this.
2) The developed torque T_{ei} of an SRM expressed in (2) is similar to that of a series dc motor having high acceleration ability. Because the developed torque of the SRM is dependent on the current waveform and the phase relationship between $\partial L(\theta_r, i)/\partial\theta_r$ and i, the properly commutation instant tuning is needed to enhance the developed torque capability.
3) The SRM can be operated as an SRG by setting the commutation instant be located in a negative inductance slope region. For an SRG, the negative back EMF will assist the increase of a winding current rate. Hence, the successful winding current control becomes more challenging.
4) Current-controlled PWM switching approaches. The HCCPWM scheme is robust against the system disturbances. Hence, it is employed for the established SRM drive shown in Fig. 1(a). In a motoring mode, the switches (S_1, S_3, S_5, S_7) are in charge of PWM switching control, while (S_2, S_4, S_6, S_8) are commutation switches. As to the generator mode, the upper and lower switches in the same leg are simultaneously operated.

Fig. 2(a) depicts the conceptual configuration of the SRM-driven flywheel, and Fig. 2(b) shows the winding inductance profile and the motor/generator operation modes. Assumed that the mechanical system losses and the SRM losses are neglected, the developed torques and the air-gap powers of the SRM in flywheel charging motor mode and discharging generator mode can be expressed from (2) as

1) Charging motor mode: $P_{df} = P_g = T_e\omega_r, P_g > 0$, $T_e > 0$.
2) Discharging generator mode: $P_{df} = P_g = T_e\omega_r, T_e < 0$, $P_g < 0$.

The per-phase HCCPWM system configuration for generating the PWM signal of phase A, the winding equivalent circuits, and currents during PWM ON and OFF intervals under the motoring mode are shown in Fig. 2(c). And the ones for the generating mode are depicted in Fig. 2(d), where the hard free-wheeling mode is adopted (the switches S_1 and S_2 are operated simultaneously) for counteracting the adverse back EMF effect, which is negative under generating operation.

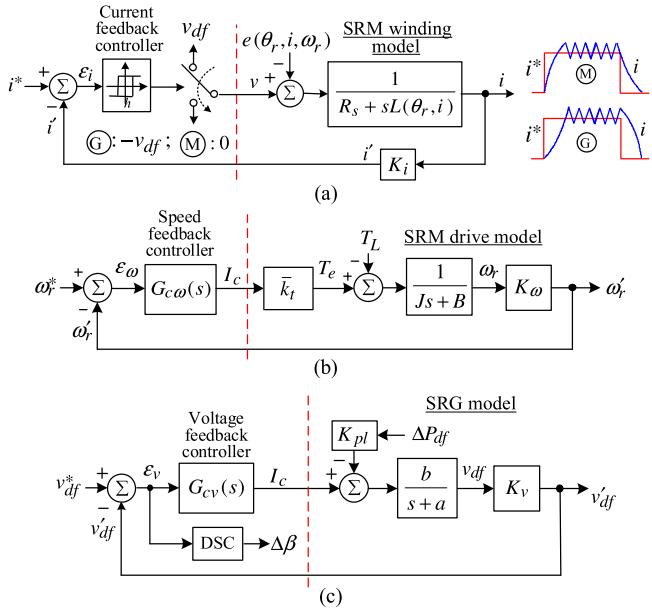

Fig. 4. Equivalent control blocks. (a) Phase winding current control loop. (b) SRM drive speed control loop. (c) SRG voltage control loop.

C. Dynamic Modeling

As mentioned previously, the winding PWM switching controlled current waveforms of an SRM are greatly affected by the back EMF, especially for the SRG owing to the negative value of back EMF. To yield robust current control, the hysteresis current controller is adopted for both SRM and SRG in the developed SRM-driven flywheel. As shown in Fig. 2(c) and (d), the soft freewheeling is adopted for the SRM drive, whereas the SRG employs the hard freewheeling to against the back EMF effects. Fig. 4(a) shows the equivalent current-loop control block.

III. Establishment of the SRM-Driven Flywheel System

A. SRM Drive

The established flywheel SRM and its converter are shown in Fig. 1(a). The major system components are described as follows.

1) Flywheel: Its photo and dimensions are shown in Fig. 1(b). The calculated moment of inertia is $J = 0.243379\,\text{kg}\cdot\text{m}^2$.
2) SRM: DENSEI motor RA130135, four-phase, 8/6, 6000 r/min, 490 W, 0.78 Nm. The measured winding dc resistance is $R_s = 0.0582\ \Omega$. And the winding inductance profile using the LCR meter (Hioki 3532-50 LCR HiTESTER) at 100 Hz is shown in Fig. 3.
3) Converter: The asymmetric bridge converter is formed using the power MOSFET IRFP4368PBF [75 V/195 A (continuous), 350 A (peak)], and the power diode DSEI120-06 A [600 V/77 A (continuous), 100 A (peak)] manufactured by International Rectifier.
4) Rotor position sensing scheme: Two-phase Hall sensors.

5) The DSP TMS320F28335 (Texas Instruments) with properly designed sensing and conditioning circuits is used to construct the digital control environment.
6) DC-link voltage filter: The dc-link filtering capacitor is chosen according to the following two guidelines: 1) PWM ripple component Δv_{dh} is reduced by choosing the capacitor with lower equivalent series resistance (ESR) at switching frequency; and 2) the total value of C_{df} is determined according to the specified lower frequency stroke ripple component Δv_{df}. Hence, C_{df} is formed by the parallel connection of a large capacitor s $C_{df1} = 20\,000\,\mu$F and a small one $C_{df2} = 220\,\mu$F with measured ESRs:

$C_{df} = C_{df1}//C_{df2} = 20\,220\mu$F/50 V, ESR = 7.97 m$\Omega$/100 Hz, 6.83 m$\Omega$/1 kHz, 6.73 m$\Omega$/1.8 kHz, 18.13 m$\Omega$, 100 kHz.

At an operating condition (motor speed $\omega_r = 4000$ r/min, stroke ripple frequency $f_{\rm st} = 1.8$ kHz, flywheel dc-link voltage $V_{df} = 24$ V, dc-link load resistance $R_{df} = 1.86\,\Omega$, dc-link power $P_{df} = 309$ W, and dc-link load current $I_{df} = 12.88$ A), the dc-link ripple voltage can be found as [30]

$$\Delta v_{df} \cong \sqrt{\left(\frac{2V_{df}R_s}{R_{df}}\right)^2 + \left(\frac{V_{df}}{\omega_{\rm st}R_{df}C_{df}}\right)^2} = 0.18\,\text{V}. \quad (3)$$

1) Speed Loop of a Flywheel Motor Under a Charging Mode: Analogous to the conventional motor drive, the speed-loop dynamic behavior of the SRM drive is approximately expressed by the block diagram in Fig. 4(b). Owing to the nonlinear torque generating characteristic, the linearized torque generating constant $\bar{k}_t$ is derived from (2). By assuming ideal current PWM control with $i_i \approx I_c$, The linearization approach is applied at a chosen operating point with $I_c = I_{c0}$ to yield

$$\Delta T_e = \bar{k}_t \Delta I_c, \bar{k}_t = I_{c0}\frac{\partial L(I_{c0}, \theta_r)}{\partial \theta_r}. \quad (4)$$

2) Voltage Loop of a Flywheel Generator Under a Discharging Mode: From Fig. 1(a), the SRG output voltage response due to the flywheel discharging is modeled as the control block depicted in Fig. 4(c). The SRG dynamic model is represented by a first-order process and a load power disturbance constant K_{pl}. For obtaining the improved generating performance, a dynamic shift controller (DSC) is developed to yield the dynamic commutation shift angle, which is adapted with the averaged voltage tracking error.

3) Commutation Instant Shift: For an SRM-driven flywheel, it will be operated both as a motor and a generator. Hence, proper commutation instant setting and shifting are important to yield better operating characteristics. The key variables in the commutation processes of an SRM and an SRG are shown in Figs. 1(c) and 3 and defined as

$\theta_{\rm on}$ = turn-ON angle;
$\theta_{\rm off}$ = turn-OFF angle;
θ_g = basic receded shift angle for SRG operation;
$\theta'_{\rm on} = \theta_{\rm on} - \beta$ = shifted turn-ON angle;
$\theta'_{\rm off} = \theta_{\rm off}$ = shifted turn-OFF angle;
$\theta_d \triangleq \theta'_{\rm off} - \theta'_{\rm on}$ = dwell angle;

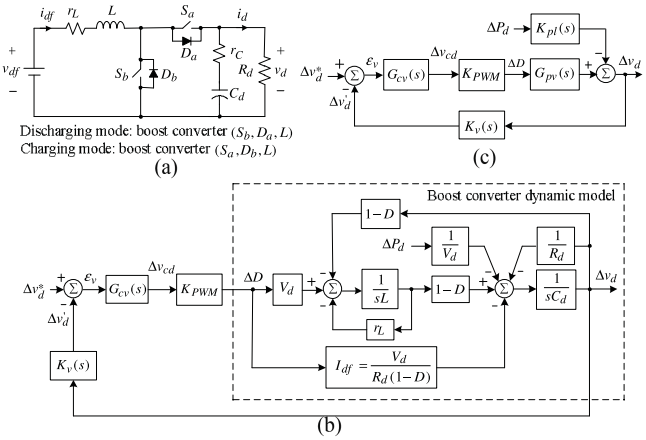

Fig. 5. Dynamic modeling of the bidirectional interface converter in the boost dc–dc converter mode. (a) Schematic. (b) Dynamic model block using the state-averaging approach. (c) Voltage-loop dynamic model.

β_1 = basic commutation shift angle: 1) $\beta_1 = \beta_m$ for SRM operation and 2) $\beta_1 = \beta_g$ for SRG operation;
$\Delta\beta$ = dynamic commutation shift angle generated from the DSC;
$\beta = \beta_1 + \Delta\beta$ = commutation shift angle: "+" for advanced shift and "−" for receded shift.

Obviously if the simultaneous shifts of $\theta_{\rm on}$ and $\theta_{\rm off}$ are applied, the dwell angle θ_d will be a constant ($\theta_d = 15^\circ$). On the other hand, for the advanced shift of $\theta_{\rm on}$ with fixed $\theta_{\rm off}$, $\theta_d > 15^\circ$ will be resulted. To let the SRM be operated in the generator mode, the commutation instants of $\theta_{\rm on}$ and $\theta_{\rm off}$ are simultaneously shifted backward by a basic shift angle of $\beta_g = -20^\circ$.

B. Control Schemes in a Charging Motoring Mode

1) HCCPWM Scheme: In the proposed current control scheme shown in Figs. 1(c) and 4(a), the HCCPWM switching scheme with soft free-wheeling is adopted with the hysteresis band being set as $h = 0.05I_c$. The digital current control sampling frequency is set to be $f_{si} = 60$ kHz. And the current sensing transfer function is set as

$$K_i(s) = \frac{K_i}{1 + \tau_i s} = \frac{0.03}{1 + 1.59 \times 10^{-5}\,\text{s}} \quad (5)$$

where $K_i = 0.3$ V/A is the sensing transfer factor, and $(1/(1 + 1.59 \times 10^{-5}\,\text{s}))$ is a low-pass filtering process with cutoff frequency $f_{ci} = 10$ kHz. Within the main dynamic frequency range, it is reasonable to assume that $i' = K_i(s)i \approx K_i i$, as shown in Fig. 4(a).

2) Speed Control Scheme: Due to the inherent high inertia load with sluggish dynamic response requirement, the PI feedback controller is adopted here as follows:

$$G_{c\omega}(s) = 12 + \frac{0.29}{s}. \quad (6)$$

The digital speed control sampling frequency is set to be $f_{s\omega} = 6$ kHz.

3) Commutation Shift Mechanism: As generally recognized, the phase current cannot track its command under higher speed

owing to back EMF effects. The voltage boosting and commutation shift can be applied to improve the tracking performance. The advanced commutation shift angle β under the charging mode is labeled in Fig. 3.

C. Control Schemes in a Discharging Generating Mode

1) HCCPWM Scheme: As indicated in Fig. 2(d), the HCCPWM scheme (band $h = 0.05I_c$) with hard free-wheeling is adopted.

2) Voltage Control Scheme: For simplicity, the voltage feedback controller shown in Fig. 4(c) is chosen to be PI type. Under a flywheel discharging period, the SRG-driven speed will be decreased gradually. The quantitative controller design is rather difficult to achieve. Hence, the trail-and-error approach according to the experimental experience is made to set

$$G_{cv}(s) = 10 + \frac{6}{s}. \tag{7}$$

The outer voltage loop digital sampling frequency is set as $f_{sv} = 6\,\text{kHz}$.

3) Commutation Shift Mechanism: The SRM-driven flywheel may hardly generate power at lower speed and/or heavier load. The commutation shift must be properly made to yield improved generating characteristics. First, the basic backward shift $\beta_g = -20^\circ$ is applied to place the winding current in the negative inductance slope area. Then, the DSC shown in Figs. 1(c) and 4(c) is used to enhance the flywheel power generating capability. The average value $\bar{\varepsilon}_v$ is obtained by a low-pass filter $H_{\text{LP}}(s)$.Then, a dynamic commutation shift angle $\beta = G_{cs}(s)\bar{\varepsilon}_v$ is generated and employed for shifting the turn-ON and turn-OFF angles simultaneously. The P-type dynamic control ($G_{cs}(s) = K_{Ps}$) is adopted here to avoid the control effort saturation caused by the remaining tracking error, which can be eliminated by the feedback controller $G_{cv}(s)$. The generated voltage command is set as $v_{df}^* = 24$ V and the key parameters of the proposed DSC are set as

$$G_{cs}(s) = K_{Ps} = 0.005 \tag{8}$$

$$H_{\text{LP}}(s) = \frac{1}{1+\tau_s s}, \quad \tau_s = \frac{1}{2\pi \times 20} = 0.008\,\text{s}. \tag{9}$$

4) Discharging Methods: From the above-mentioned analyses for the SRM-driven flywheel, one can be aware the following facts: 1) the flywheel driving speed will be gradually decreased during the discharging process; and 2) the speed-dependent SRM back EMF will be reduced accordingly. The generated voltage command must be properly set and the commutation instant must also be tuned to yield the improved discharging characteristics.

The possible discharging approaches are suggested as follows.

1) Fixed voltage control mode without the DSC: the constant voltage commands are set as $v_{df}^* = 24\,\text{V}$ and $v_d^* = 48\,\text{V}$. Only the basic backward shift $\beta_g = -20^\circ$ is applied.
2) Fixed voltage control mode with the DSC: the same as 1) but the tuning for commutation instant by the proposed DSC scheme is added.

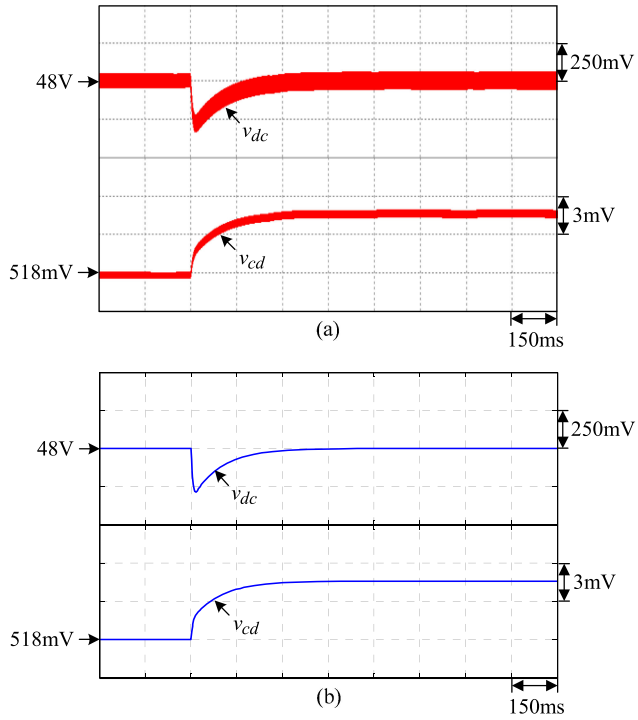

Fig. 6. Simulated (v_d, v_{cd}) of the established dc–dc boost converter due to a step load resistance change $R_{\text{dc}} = 5.91$ to $4.7\,\Omega$ by the designed voltage controller. (a) Based on the circuit using the PSIM software. (b) Based on the derived state-averaging dynamic model using the MATLAB.

3) Speed adapted voltage command control mode: the generated voltage command v_{df}^* is decreased with the reduced speed.
4) Tracking error adapted voltage command control mode: as shown in Fig. 1(b), the voltage command is modified by a component of Δv_{df}^*, which is yielded by regulating the filtered voltage tracking error through a PI controller.

Due to the limit of scope, only the first two approaches are conducted here.

IV. Bidirectional DC–DC Interface Converter

In the bidirectional dc–dc boost–buck interface converter depicted in Fig. 1(a), it is operated as a buck converter from v_d to v_{df} by (L, S_a, D_b) during flywheel charging operation. Conversely, the flywheel discharging is conducted by the boost converter from v_{df} to v_d formed by (L, S_b, D_a). The energy storage inductor L and the voltage feedback controller from G_{cv} are common for these two modes, and they all are treated in a boost converter mode.

A. Energy Storage Inductor and Power Devices

Through ripple analysis, the inductor $L = 120\,\mu\text{H}$ is chosen here. It is wound using the wire of AWG#10 with 25 turns on a toroidal core T249-26 (Micrometals). The measured inductances of the inductor are ($132.09\,\mu\text{H}/60\,\text{Hz}$), ($127.47\,\mu\text{H}/20\,\text{kHz}$), and ($126.92\,\mu\text{H}/30\,\text{kHz}$). The same

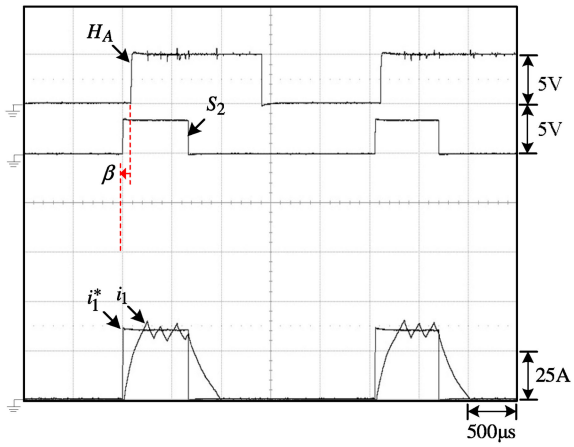

Fig. 7. Measured, switch signal S_2, winding current i_1, and its command i_1^* of the SRM drive by the HCCPWM scheme with hysteresis band $h = 0.05I_c$ and ($v_d = 48$ V, $v_{df} = 32$ V) at ($\omega_r^* = 4000$ r/min, $\beta = 3°$).

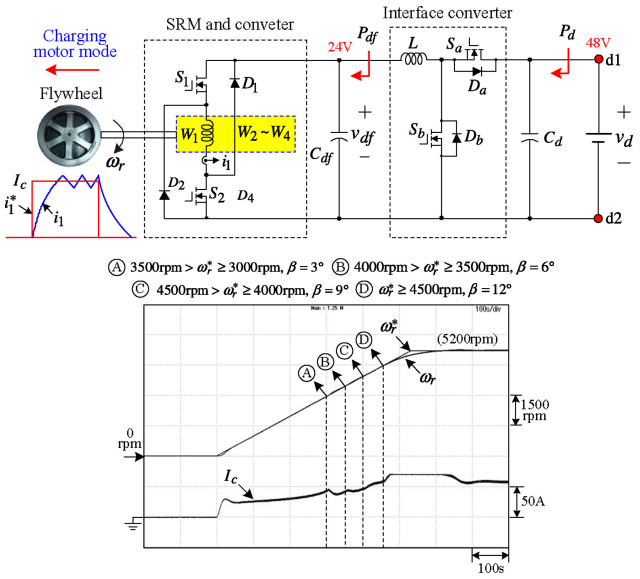

Fig. 8. Measured (ω_r^*, ω_r') and I_c of the SRM-driven flywheel during the charging process due to the ramp speed command of $\omega_r = 0 \rightarrow 5200$ r/min with ($v_d = 48$ V, $v_{df} = 32$ V) and i) $\omega_r \leq 3000$ r/min: $\beta = 0°$; ii) 3000 r/min $\leq \omega_r \leq 3500$ r/min: $\beta = 3°$; iii) 3500 r/min $\leq \omega_r \leq 4000$ r/min: $\beta = 6°$; iv) 4000 r/min $\leq \omega_r \leq 4500$ r/min: $\beta = 9°$; and v) 4500 r/min $\leq \omega_r$: $\beta = 12°$.

power devices as those of the SRM converter listed above are adopted here.

B. Control Scheme

The bidirectional interface converter shown in Fig. 1(a) is repeatedly depicted in Fig. 5(a). For simplicity and due to the sluggish response attribute possessed by the highly inertia load type of the flywheel, the direct duty-ratio control mode without current control is adopted for the both boost and the buck converters. The dynamic modeling using the state-averaging method and the controller design for the boost dc–dc converter in the discharging mode are made. And the designed controller is also suited for the buck dc–dc converter in the charging mode.

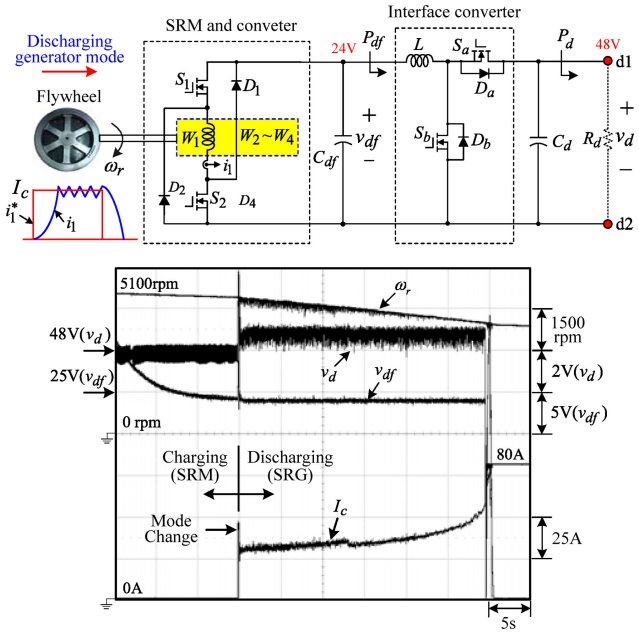

Fig. 9. Measured ω_r, v_{df}, v_d, and I_c of the SRM-driven flywheel under the discharging mode with a fixed voltage control mode without the DSC ($\beta_g = -20°$, $\beta = 0°$) at $R_d = 22\,\Omega$.

1) Dynamic Modeling: Some assumptions are made in physical modeling deviation: 1) the power devices are ideal; 2) continuous-current mode operation; and 3) the ESR of energy storage inductor L is denoted by r_L, while the ESR r_C of C_d is neglected. Applying the state-averaging approach, one can derive and draw the dynamic model block, as shown in Fig. 5(b). And through rearranging, one can yield the equivalent voltage-loop control block shown in Fig. 5(c). The switching frequency is chosen as $f_s = 30$ kHz, and the voltage loop control sampling rate is also set as $f_{sv} = 30$ kHz. The related transfer function can be derived from Fig. 5(b) as follows:

$$G_{pv}(s) \triangleq \frac{\Delta v_d(s)}{\Delta D(s)} = \frac{-LI_{df}R_d s + [R_d^2(1-D)V_d - I_{df}r_L]}{R_d^2 C_d L s^2 + C_d r_L R_d^2 s + (1-D)^2 R_d^2} \tag{10}$$

$$K_{pl}(s) \triangleq \frac{\Delta v_d}{\Delta P_d} = \frac{-LR_d s - r_L R_d}{V_d[LC_d R_d s^2 + (C_d r_L R_d + L)s + r_L + R_d(1-D)^2]}. \tag{11}$$

The set system parameters are $L = 126.92\,\mu$H, $r_L = 50\,$mΩ, $C_d = 51.7$ mF, $f_s = 30$ kHz, and $K_{\mathrm{PWM}} = 1$. At a given operating point ($V_d = 48$ V, $V_{df} = 24$ V, $D = 0.5$, $R_d = 5.91\,\Omega$), the dynamic model transfer functions found from (10) and (11) are

$$G_{pv}(s) \triangleq \frac{\Delta v_d(s)}{\Delta D(s)} = \frac{-0.0122s + 873.46}{0.0002s^{2+}0.0903s + 8.732} \tag{12}$$

$$K_{pl}(s) \triangleq \frac{\Delta v_d}{\Delta P_d} = \frac{-0.0008s - 0.296}{0.0019s^2 + 0.74s + 73.32}. \tag{13}$$

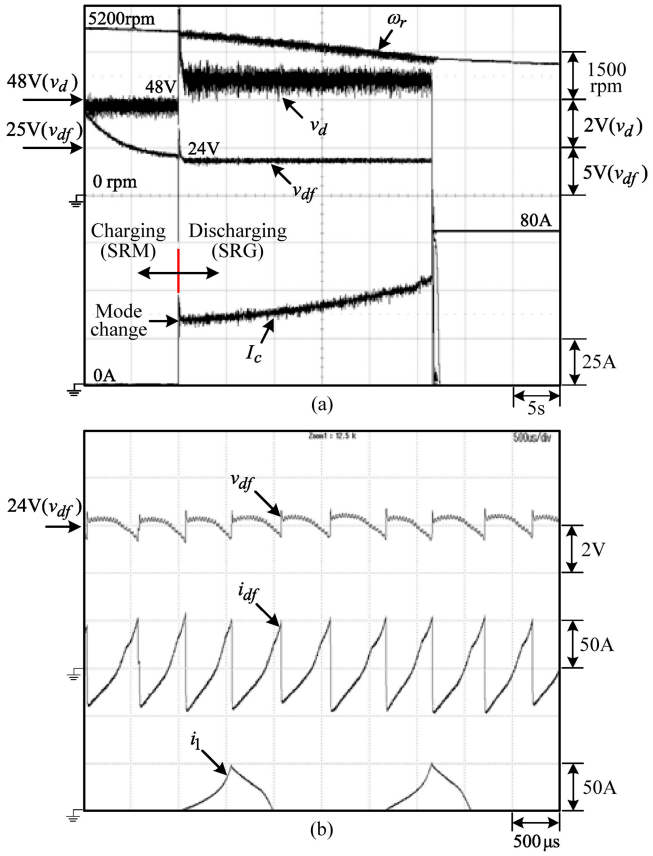

Fig. 10. Measured results of the SRM-driven flywheel under the discharging mode with a fixed voltage control mode without the DSC ($\beta_g = -20°, \beta = 0°$) at $R_d = 22\,\Omega$. (a) ω_r, v_{df}, v_d, and I_C. (b) v_{df}, i_{df}, and i_1.

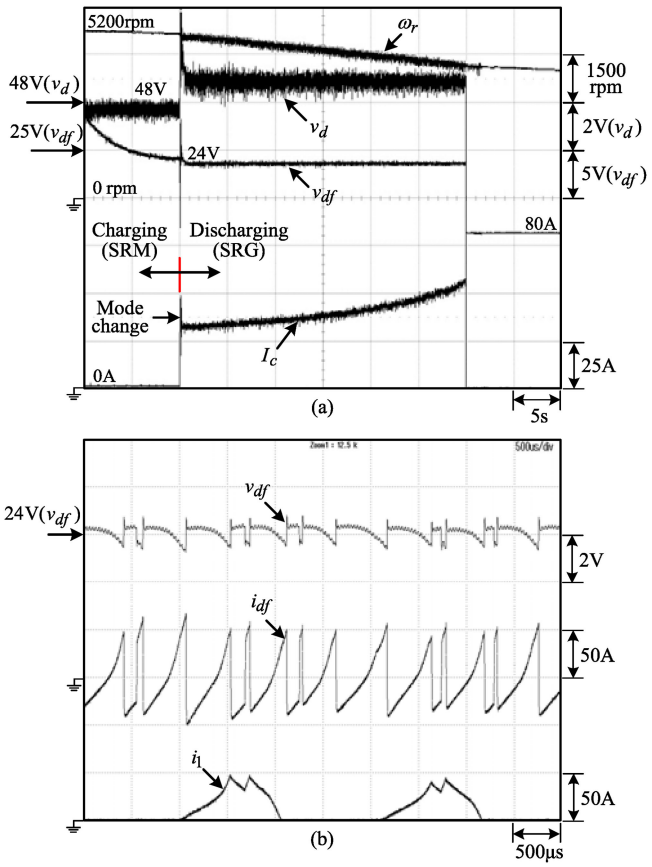

Fig. 11. Measured results of the SRM-driven flywheel under the discharging mode with a fixed voltage control mode and DSC ($\beta_g = -20°$, β varied by the DSC) at $R_d = 22\,\Omega$. (a) ω_r, v_{df}, v_d, and I_C. (b) v_{df}, i_{df}, and i_1.

2) Feedback Control: The voltage sensing factor is set as

$$K_v(s) = \frac{K_v}{1+\tau_v s} = \frac{0.05}{1+0.0001s}. \tag{14}$$

Based on the dynamic model established in Fig. 5(b) and (c) with the transfer functions listed in (11) and (12), the PI feedback controller is determined via computer-aided simulation to be

$$G_{cv}(s) = K_{Pv} + \frac{K_{Iv}}{s} = 0.1 + \frac{3}{s}. \tag{15}$$

In the dc–dc boost converter shown in Fig. 1(a), the input dc voltage is set as $v_{df} = 24$ V, and the dc output voltage command is set as $v_d^* = 48$ V. Fig. 6(a) shows the simulated output voltage v_d and the resulted control effort v_{cd} due to a step load resistance change of $R_d = 5.91$ to $4.7\,\Omega$ ($\Delta P_d = 100$ W, $P_d = 390$ W $\rightarrow$ 490 W) based on the circuit shown in Fig. 5(a) using the PSIM software. And the simulated results based on the control block of Fig. 5(b) and (c) using the MATLAB software are plotted in Fig. 6(b). The results shown in Fig. 6(a) and (b) confirm their closeness.

The designed controller listed in (15) is also applied for this interface converter in the buck mode for regulating the voltage v_{df}, as shown in Fig. 1(c).

TABLE I
MEASURED STEADY-STATE CHARACTERISTICS OF THE SRM-DRIVEN FLYWHEEL AT DIFFERENT SPEEDS

ω_r	1000 r/min	1000 r/min	4000 r/min
β	0°	3°	3°
v_d	48 V	48 V	48 V
P_d	28.6 W	28 W	390.3 W
v_{df}	24 V	24 V	32 V
P_{df}	23.6 W	23.8 W	361 W
$\eta = (P_{df}/P_d)$	82.52%	85%	92.49%

V. CHARGING AND DISCHARGING OPERATIONS

A. Flywheel Charging

In the established SRM-driven flywheel control scheme shown in Fig. 1(c), by setting all switches in the position "M," the system is operated in the motor mode to establish the flywheel speed. The effects of commutation advanced shift and voltage boosting are first comprehended experimentally. With $v_d = 48$ V, the measured steady-state characteristics of the SRM-driven flywheel at different speeds, v_{df}, and shift angles β are listed in Table I. All these powers are measured using the digital power meter WT1600M manufactured by YOKOGAWA, Japan. Under ($v_d = 48$ V, $v_{df} = 32$ V) and ($\omega_r = 4000$ r/min, $\beta = 3°$), Fig. 7 shows the measured (i_1^*, i_1) of phase-1

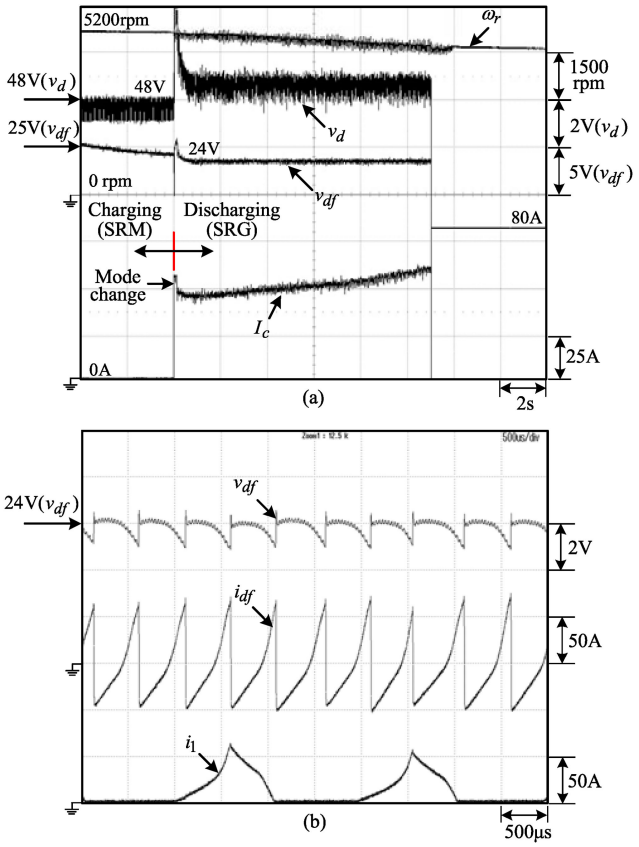

Fig. 12. Measured results of the SRM-driven flywheel under the discharging mode with the DSC at $R_d = 11.76\,\Omega$. (a) ω_r, v_{df}, v_d, and I_C. (b) v_{df}, i_{df}, and i_1.

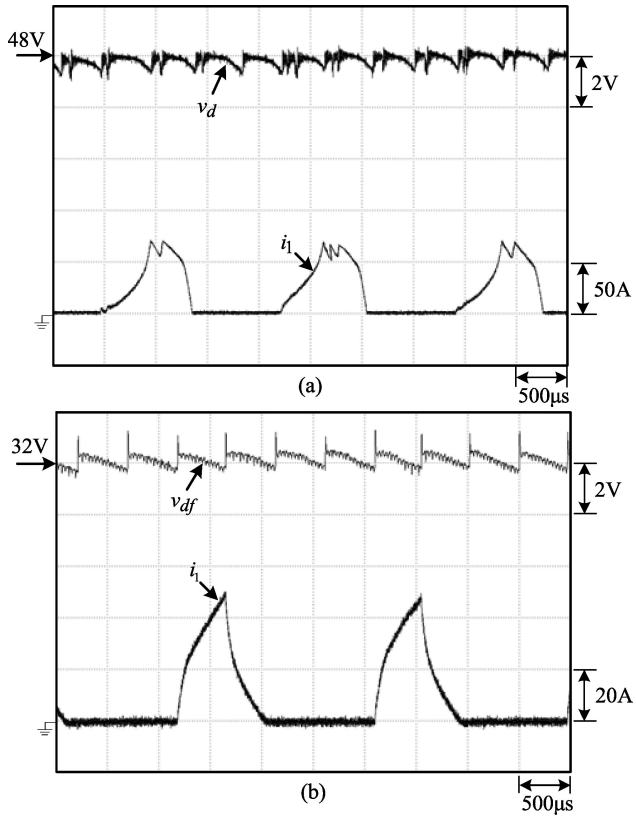

Fig. 13. Measured results of the SRM-driven flywheel being charged from the SRG. (a) v_d and i_1 of the SRG. (b) v_{df} and i_1 of the SRM-driven flywheel.

winding, Hall signal H_A, and switching signal S_A. Good PWM-controlled winding current waveform is seen.

The results shown in Table I and Fig. 7 indicate that the proper commutation shift and voltage boosting are the key issues to achieve a high-performance SRM drive over a wide speed range. Accordingly, to let the SRM-driven flywheel be smoothly accelerated, the voltages ($v_d = 48\,\text{V}, v_{df} = 32\,\text{V}$) are set, and the shift angles β under various speeds are arranged as

1) $\omega_r \le 3000$ r/min: $\beta = 0°$;
2) 3000 r/min $\le \omega_r \le 3500$ r/min: $\beta = 3°$;
3) 3500 r/min $\le \omega_r \le 4000$ r/min: $\beta = 6°$;
4) 4000 r/min $\le \omega_r \le 4500$ r/min: $\beta = 9°$; and
5) 4500 r/min $\le \omega_r$: $\beta = 12°$.

The measured (ω_r^*, ω_r') and I_c due to the ramp speed command change $\omega_r = 0 \rightarrow 5200$ r/min are plotted in Fig. 8. The smooth flywheel acceleration characteristics are observed.

B. Flywheel Discharging

The switches in the SRM-driven flywheel control scheme shown in Fig. 1(c) are placed in position "G." The controllers of the SRM drive in the generator mode and the bidirectional dc–dc interface converter have been presented previously.

1) Fixed Voltage Control Mode Without the DSC: The current command limit is set to be $I_{c(\max)} = 80$ A, and the commutation angles are set as $\beta_g = -20°$ and $\beta = 0°$. Let ($v_{df}^* = 24$ V, $v_d^* = 48$ V), the initial speed $\omega_r = 5100$ r/min and $R_d = 22\,\Omega$, Fig. 9 shows the measured rotor speed ω_r, two dc-link voltages (v_{df}, v_d), and the resulted current command magnitude I_c during discharging operation. The schematic with measured variables being labeled is also shown in Fig. 9. The power flow and the measured variables during the SRM-driven flywheel discharging process can be clearly observed. Normal discharging characteristics are observed.

2) Fixed Voltage Control Mode With the DSC: Some measured results are provided to demonstrate the effectiveness of the DSC. Fig. 10 shows the measured results of the SRM-driven flywheel under the discharging mode without the DSC at $R_d = 20\,\Omega$. Under the same condition, Fig. 11 shows the measured results with the DSC. From Figs. 10 and 11, one can find that with the DSC, the winding current waveforms become better and the longer discharging periods are yielded. Now let $R_d = 11.76\,\Omega$, only the SRG system with the DSC can be operated in discharging operation with its results being plotted in Fig. 12. All steady-state characteristics corresponding to Figs. 10–12 are listed in Table II. The maximum discharging power is found to be $P_{df} = 226.5$ W.

VI. SRG-Based DC Microgrid Supported by SRM-Driven Flywheel Storage

The established SRM-driven flywheel is connected to the wind SRG-based dc microgrid, as shown in Fig. 1(a). It can be charged from the wind SRG output dc bus to establish its

TABLE II
MEASURED STEADY-STATE CHARACTERISTICS OF THE SRM-DRIVEN FLYWHEEL UNDER DIFFERENT LOAD CONDITIONS

	Without DSC			With DS		
R_d	20 Ω	15.38 Ω	11.76 Ω	20 Ω	15.38 Ω	11.76 Ω
V_d	48.8 V	48.7 V	(∗)	48.9 V	48.8 V	48.8 V
P_d	117 W	152.8 W	(∗)	118 W	153 W	201.8 W
V_{df}	23.7 V	23.8 V	(∗)	23.9 V	23.8 V	24 V
P_{df}	132 W	171.3 W	(∗)	136 W	170.9 W	226.5 W
$\eta(P_d/P_{df})$	88.63%	89.2%	(∗)	86.76%	89.53%	89.09%

∗Failed operation.

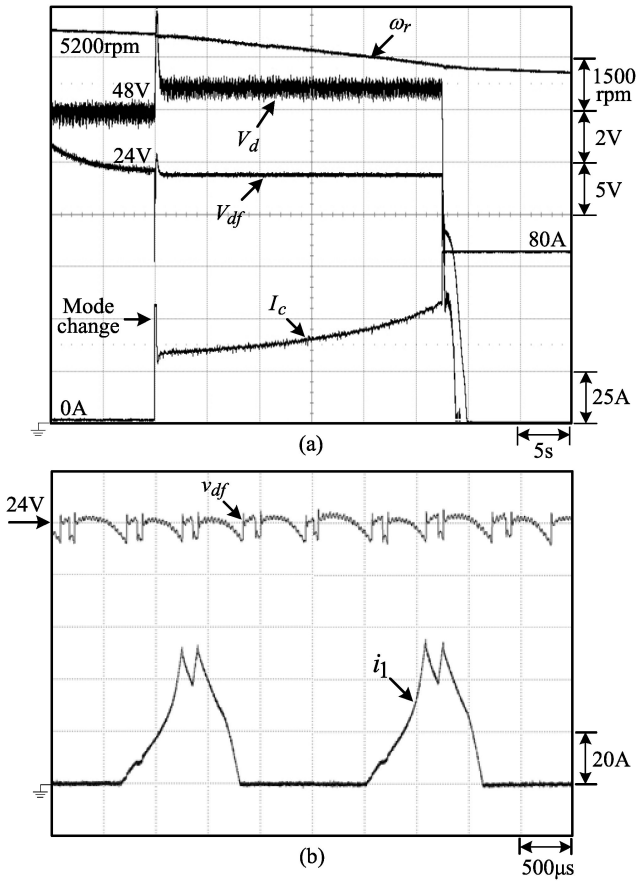

Fig. 14. Measured results of the SRM-driven flywheel under the discharging mode. (a) ω_r, v_{df}, v_d, and I_c. (b) v_{df} and i_1.

running speed. Conversely, the flywheel can discharge its stored energy to power the dc microgrid.

A. Charging Mode

During the test, the wind SRG of microgrid powers the three-phase load inverter under balanced loads ($R_a = R_b = R_c = 900\,\Omega$), and it also powers the SRM-driven flywheel to establish its speed through the interface buck dc–dc converter. At a particular instant with the SRG-driven speed of $\omega_r = 6000$ r/min and the SRM-driven flywheel speed $\omega_r = 5200$ r/min, the measured dc-link voltage v_d and phase-1 winding current i_1 of the SRG are shown in Fig. 13(a), and Fig. 13(b) depicts the measured dc-link voltage v_{df} and phase-1 winding current i_1 of the

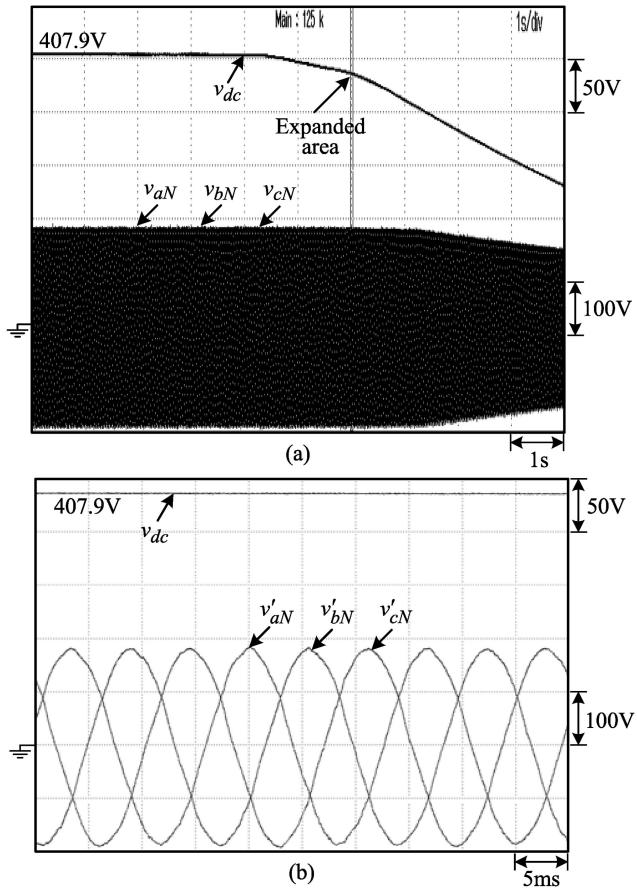

Fig. 15. Measured results of the flywheel storage discharging characteristics when the main source of the dc microgrid is suddenly removed. (a) DC-link voltage $v_{\rm dc}$ and three output voltage (v_{aN}, v_{bN}, v_{cN}) of the 3P3W load inverter at balanced loads of ($R_a = R_b = R_c = 900\,\Omega$). (b) Expanded waveforms of (a).

SRM-driven flywheel. The measured steady-state key system variables are

1) SRM-driven flywheel interface buck dc–dc converter: $V_d = 47.7$ V, $P_d = 743.3$ W, $V_{df} = 31.73$ V, $P_{df} = 704.9$ W, $\eta \equiv P_{df}/P_d = 94.83\%$; and
2) SRG followed interface interleaved CFPP dc–dc converter: $P_d = 122.3$ W, $V_d = 47.7$ V, $V_{\rm dc} = 404.7$ V, $P_{\rm dc} = 85.55$ W, $\eta \equiv P_{\rm dc}/P_d = 69.95\%$.

Normal operations of wind SRG and SRM in the flywheel system can be observed from the winding current waveforms. And reasonable energy conversion efficiencies of the interface dc–dc converters can also be found from the measured results.

B. Discharging Mode

The SRG is first operated stably under $\omega_r = 6000$ r/min, then the main source of the SRG in the dc microgrid is suddenly removed, and the flywheel storage discharging is activated simultaneously. The measured terminal voltage v_{df}, microgrid dc-link voltage v_d actual speed ω_r, and current command I_c are shown in Fig. 14(a), and the dc-link voltage v_{df} and phase-1 winding current i_1 of the SRM-driven flywheel are shown in Fig. 14(b). In addition, the measured microgrid dc-link voltage

v_d and load inverter output voltage waveforms (v_{aN}, v_{bN}, v_{cN}) are shown in Fig. 15(a), and Fig. 15(b) plots their magnifications at a particular time instant. The results indicate that within a short time period, the microgrid can be supported by the energy from the flywheel, and the load inverter output waveform quality is maintained. The measured key system variables are

1) SRM-driven flywheel interface boost dc–dc converter: $V_{df} = 23.97\,\text{V}$, $P_{df} = 146.2\,\text{W}$, $V_d = 48.88\,\text{V}$, $P_d = 123\,\text{W}$, $\eta = P_d/P_{df} = 84.13\%$; and

2) SRG followed interleaved CFPP dc–dc boost converter: $V_d = 48.88\,\text{V}$, $P_d = 123\,\text{W}$, $V_{\text{dc}} = 407.9\,\text{V}$, $P_{\text{dc}} = 83.6\,\text{W}$, $\eta = P_{\text{dc}}/P_d = 67.95\%$.

VII. Conclusion

This paper has developed an SRM-driven flywheel system and performed its charging and discharging operation controls. The SRM with an asymmetric converter is first properly designed and controlled to yield good winding current control characteristics. The flywheel system is interfaced to the wind SRG output via a half-bridge bidirectional dc–dc converter with a properly designed controller. It is operated in the buck mode under the flywheel charging mode and in the boost mode under the flywheel discharging mode. In the charging SRM motor mode, the programmed commutation shifts adapted to the flywheel changing speeds are set to yield smooth acceleration characteristics. As to the flywheel discharging mode, the dynamic commutation shift approach is developed to automatically adjust the shift angle according to the average voltage tracking error. The effectiveness of the proposed control approaches and the operation performances of the established SRM-driven flywheel were first verified experimentally. Then, it is interconnected to a wind SRG-based dc microgrid, and some measured results are provided to demonstrate the satisfactory operation characteristics.

References

[1] T. Dragicevic, X. Lu, J. C. Vasquez, and J. M. Guerrero, "DC microgrids—Part II: A review of power architectures, applications, and standardization issues," *IEEE Trans. Power Electron.*, vol. 31, no. 5, pp. 3528–3549, May 2016.

[2] V. A. Boicea, "Energy storage technologies: The past and the present," *Proc. IEEE*, vol. 102, no. 11, pp. 1777–1794, Nov. 2014.

[3] M. Farhadi and O. Mohammed, "Energy storage technologies for high-power applications," *IEEE Trans. Ind. Appl.*, vol. 52, no. 3, pp. 1953–1961, May/Jun. 2016.

[4] E. Chemali, M. Preindl, P. Malysz, and A. Emadi, "Electrochemical and electrostatic energy storage and management systems for electric drive vehicles state-of-the-art review and future trends," *IEEE J. Emerging Select. Topics Power Electron.*, vol. 4, no. 3, pp. 1117–1134, Sep. 2016.

[5] E. Chatzinikolaou and D. J. Rogers, "A comparison of grid-connected battery energy storage system designs," *IEEE Trans. Power Electron.*, vol. 32, no. 9, pp. 6913–6923, Sep. 2017.

[6] R. Pena-Alzola, R. Sebastian, J. Quesada, and A. Colmenar, "Review of flywheel based energy storage systems," in *Proc. IEEE Power Eng.*, 2011, pp. 1–6.

[7] G. O. Suvire, M. G. Molina, and P. E. Mercado, "Improving the integration of wind power generation into ac microgrids using flywheel energy storage," *IEEE Trans. Smart Grid*, vol. 3, no. 4, pp. 1945–1954, Dec. 2012.

[8] J. Itoh, D. Sato, T. Nagano, K. Tanaka, N. Yamada, and K. Kato, "Development of high efficiency flywheel energy storage system for power load-leveling," in *Proc. IEEE 36th Int. Telecommun. Energy Conf.*, 2014, pp. 1–8.

[9] B. Sun, T. Dragicevic, F. D. Freijedo, J. C. Vasquez, and J. M. Guerrero, "A control algorithm for electric vehicle fast charging stations equipped with flywheel energy storage systems," *IEEE Trans. Power Electron.*, vol. 31, no. 9, pp. 6674–6685, Sep. 2016.

[10] W. Gruber, T. Hinterdorfer, H. Sima, A. Schulz, and J. Wassermann, "Comparison of different motor-generator sets for long term storage flywheels," in *Proc. IEEE Power Electron., Electr. Drives, Autom. Motion*, 2014, pp. 161–166.

[11] M. Mansour, S. Rachdi, M. N. Mansouri, and M. F. Mimouni, "Direct torque control strategy of an induction-machine-based flywheel energy storage system associated to a variable-speed wind generator," *Energy Power Eng.*, vol. 4, pp. 255–263, 2012.

[12] S. Ghosh and S. Kamalasadan, "An energy function-based optimal control strategy for output stabilization of integrated DFIG-flywheel energy storage system," *IEEE Trans. Smart Grid*, vol. 8, no. 4, pp. 1922–1931, Jul. 2017.

[13] H. H. Abdeltawab and Y. I. Mohamed, "Robust energy management of a hybrid wind and flywheel energy storage system considering flywheel power losses minimization and grid-code constraints," *IEEE Trans. Ind. Electron.*, vol. 63, no. 7, pp. 4242–4254, Jul. 2016.

[14] S. R. Gurumurthy, V. Agarwal, and A. Sharma, "A novel dual-winding BLdc generator-buck converter combination for enhancement of the harvested energy from a flywheel," *IEEE Trans. Ind. Electron.*, vol. 63, no. 12, pp. 7563–7573, Dec. 2016.

[15] J. I. Itoh, T. Masuda, D. Sato, T. Nagano, T. Suzuki, and N. Yamada, "Development of magnetic assist system in flywheel energy storage system for power load-leveling," in *Proc. IEEE Int. Conf. Renew. Energy Res. Appl.*, 2016, pp. 198–203.

[16] H. A. Moghaddam, A. Vahedi, and S. H. Ebrahimi, "Design optimization of transversely laminated synchronous reluctance machine for flywheel energy storage system using response surface methodology," *IEEE Trans. Ind. Electron.*, vol. 64, no. 12, pp. 9748–9757, Dec. 2017.

[17] R. Cardenas, R. Pena, M. Perez, J. Clare, G. Asher, and P. Wheeler, "Power smoothing using a flywheel driven by a switched reluctance machine," *IEEE Trans. Ind. Electron.*, vol. 53, no. 4, pp. 1086–1093, Jun. 2006.

[18] E. Bernsmüller, L. G. B. Rolim, and A. C. Ferreira, "External rotor switched reluctance machine for a kinetic energy storage system," in *Proc. 42nd Annu. Conf. IEEE Ind. Electron. Soc.*, 2016, pp. 1636–1641.

[19] P. C. Sen, *Principles of Electric Machines and Power Electronics*, 2nd ed. Hoboken, NJ, USA: Wiley, 1997.

[20] R. Krishnan, *Switched Reluctance Motor Drives: Modeling, Simulation, Analysis, Design, and Applications*. New York, NY, USA: CRC Press, 2001.

[21] T. J. E. Miller, "Optimal design of switched reluctance motors," *IEEE Trans. Ind. Electron.*, vol. 49, no. 1, pp. 15–27, Feb. 2002.

[22] S. Baiming, S. M. Lukic, and A. Emadi, "A digital current control for switched reluctance motor drives," in *Proc. IEEE Int. Symp. Ind. Electron.*, 2010, pp. 1163–1168.

[23] H. Hannoun, M. Hilairet, and C. Marchand, "Design of an SRM speed control strategy for a wide range of operating speeds," *IEEE Trans. Ind. Electron.*, vol. 57, no. 9, pp. 2911–2921, Sep. 2010.

[24] J. J. Gribble, P. C. Kjaer, and T. J. E. Miller, "Optimal commutation in average torque control of switched reluctance motors," *IEE Proc., Electr. Power Appl.*, vol. 146, no. 1, pp. 2–10, 1999.

[25] K. I. Hwu and C. M. Liaw, "Intelligent tuning of commutation for maximum torque capability of a switched reluctance motor," *IEEE Trans. Energy Convers.*, vol. 18, no. 1, pp. 113–120, Mar. 2003.

[26] C. Mademlis and I. Kioskeridis, "Performance optimization in switched reluctance motor drives with online commutation angle control," *IEEE Trans. Energy Convers.*, vol. 18, no. 3, pp. 448–457, Sep. 2003.

[27] Y. G. Dessouky, B. W. Williams, and J. E. Fletcher, "A novel power converter with voltage-boosting capacitors for a four-phase SRM drive," *IEEE Trans. Ind. Electron.*, vol. 45, no. 5, pp. 815–823, Oct. 1998.

[28] H. C. Chang and C. M. Liaw, "Development of a compact switched-reluctance motor drive for EV propulsion with voltage-boosting and PFC charging capabilities," *IEEE Trans. Ind. Electron.*, vol. 58, no. 5, pp. 1763–1775, May 2011.

[29] R. Cardenas, R. Pena, M. Perez, J. Clare, G. Asher, and P. Wheeler, "Control of a switched reluctance generator for variable-speed wind energy applications," *IEEE Trans. Energy Convers.*, vol. 20, no. 4, pp. 781–791, Dec. 2005.

[30] Y. C. Chang and C. M. Liaw, "On the design of power circuit and control scheme for switched reluctance generator," *IEEE Trans. Power Electron.*, vol. 23, no. 1, pp. 445–454, Jan. 2008.

[31] N. Schofield and S. Lomg, "Generator operation of a switched reluctance starter/generator at extended speeds," *IEEE Trans. Veh. Technol.*, vol. 58, no. 1, pp. 48–56, Jan. 2009.
[32] M. Menne, R. B. Inderka, and R. W. De Doncker, "Critical states in generating mode of switched reluctance machines," in *Proc. IEEE 31st Annu. Power Electron. Spec. Conf.*, vol. 3, 2000, pp. 1544–1550.
[33] D. A. Torrey, "Switched reluctance generators and their control," *IEEE Trans. Ind. Electron.*, vol. 49, no. 1, pp. 3–14, Feb. 2002.
[34] C. Mademlis and I. Kioskeridis, "Optimizing performance in current-controlled switched reluctance generators," *IEEE Trans. Energy Convers.*, vol. 20, no. 3, pp. 556–565, Sep. 2005.
[35] F. Caricchi, F. Crescimbini, G. Noia, and D. Pirolo, "Experimental study of a bidirectional dc-dc converter for the dc link voltage control and the regenerative braking in PM motor drives devoted to electrical vehicles," in *Proc. 9th Annu. Appl. Power Electron. Conf. Expo.*, vol. 1, 1994, pp. 381–389.
[36] S. Zhang, O. Thomsen, and M. Andersen, "Optimal design of a push-pull-forward half-bridge (PPFHB) bidirectional dc-dc converter with variable input voltage," *IEEE Trans. Ind. Electron.*, vol. 59, no. 7, pp. 2761–2771, Jul. 2012.
[37] M. Yilmaz and P. T. Krein, "Review of battery charger topologies, charging power levels, and infrastructure for plug-in electric and hybrid vehicles," *IEEE Trans. Power Electron.*, vol. 28, no. 5, pp. 2151–2169, May 2013.
[38] S. S. Williamson, A. K. Rathore, and F. Musavi, "Industrial electronics for electric transportation: Current state-of-the-art and future challenges," *IEEE Trans. Ind. Electron.*, vol. 62, no. 5, pp. 3021–3032, May 2015.
[39] M. A. Khan, A. Ahmed, I. Husain, Y. Sozer, and M. Badawy, "Performance analysis of bidirectional dc-dc converters for electric vehicles," *IEEE Trans. Ind. Appl.*, vol. 51, no. 4, pp. 3442–3452, Jul./Aug. 2015.

Chi-Yuan Ho was born in Taipei, Taiwan, on August 27, 1993. He received the B.S. and M.S. degrees in electrical engineering from the National Tsing Hua University, Hsinchu, Taiwan, in 2015 and 2017, respectively.

His research interests include electric machine controls, motor drives, and power electronics.

Jung-Chi Wang was born in Taipei, Taiwan, on February 29, 1989. He received the B.S. degree in power mechanical engineering and the M.S. degree in electrical engineering from the National Tsing Hua University, Hsinchu, Taiwan, in 2011 and 2013, respectively.

Currently, he is currently a Power Engineer with Lite-On Technology Corporation, Hsinchu, Taiwan. His research interest focuses on power electronics.

Kai-Wei Hu (S'13–M'16) was born in Kaohsiung, Taiwan, on December 10, 1988. He received the B.S. and Ph.D. degrees in electrical engineering from the National Tsing Hua University, Hsinchu, Taiwan, in 2011 and 2015, respectively.

From 2011 to 2015, he was a Teaching and Research Assistant with the Department of Electrical Engineering, National Tsing Hua University, Hsinchu, Taiwan. His research interests include power electronics, self-sensing, motor drives, electric machine controls, and motor designs.

Chang-Ming Liaw (S'88–M'89) was born in Taichung, Taiwan, on June 19, 1951. He received the B.S. degree in electronic engineering from the Evening Department, Tamkang College of Arts and Sciences, Taipei, Taiwan, in 1979, and the M.S. and Ph.D. degrees in electrical engineering from the National Tsing Hua University, Hsinchu, Taiwan, in 1981 and 1988, respectively.

In 1988, he joined the faculty of the Department of Electrical Engineering, National Tsing Hua University, as an Associate Professor, and has been a Professor since 1993. His research interests include power electronics, motor drives, and electric machine controls.

Dr. Liaw is a Life Member of the Chinese Institute of Electrical Engineering, an Editor for the *International Journal of Electrical Engineering*, and an Editorial Board Member for Hindawi *Advances in Power Electronics*.